JACS
JOURNAL OF THE AMERICAN CHEMICAL SOCIETY
Article
pubs.acs.org/JACS

Metastable Layered Cobalt Chalcogenides from Topochemical Deintercalation

Xiuquan Zhou,[†] Brandon Wilfong,[†,‡] Hector Vivanco,[†] Johnpierre Paglione,[§,‡] Craig M. Brown,[∥] and Efrain E. Rodriguez*[,†,‡]

[†]Department of Chemistry and Biochemistry, University of Maryland, College Park, Maryland 20742, United States
[‡]Center for Nanophysics and Advanced Materials, University of Maryland, College Park, Maryland 20742, United States
[§]Department of Physics, University of Maryland, College Park, Maryland 20742, United States
[∥]Center for Neutron Research, National Institute of Standards and Technology, Gaithersburg, Maryland 20899, United States

Supporting Information

ABSTRACT: We present a general strategy to synthesize metastable layered materials via topochemical deintercalation of thermodynamically stable phases. Through kinetic control of the deintercalation reaction, we have prepared two hypothesized metastable compounds, CoSe and CoS, with the anti-PbO type structure from the starting compounds KCo_2Se_2 and KCo_2S_2, respectively. Thermal stability, crystal structure from X-ray and neutron diffraction, magnetic susceptibility, magnetization, and electrical resistivity are studied for these new layered chalcogenides; both CoSe and CoS are found to be weak itinerant ferromagnets with Curie temperatures close to 10 K. Due to the weak van der Waals forces between the layers, CoSe is found to be a suitable host for further intercalation of guest species such as Li-ethylenediamine. From first-principles calculations, we explain why the Co chalcogenides are ferromagnets instead of superconductors as in their iron analogues. Bonding analysis of the calculated electronic density of states both explains their phase stability and predicts the limits of our deintercalation technique. Our results have broad implications for the rational design of new two-dimensional building blocks for functional materials.

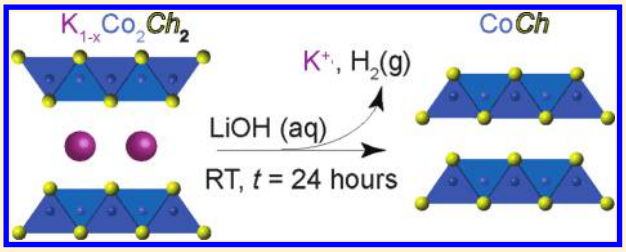

INTRODUCTION

To advance the first-principles approach toward materials discovery,[1,2] we must also develop new synthetic strategies for finding functional materials. One outstanding issue is that many predicted inorganic materials, especially extended solids, may not be thermodynamically favored. A solution to this problem is to kinetically stabilize such predicted compounds, i.e., to isolate the metastable phases. Inspired by recent work on finding metastable and superconducting iron chalcogenides,[3,4] we present topochemical methods to find metastable phases of cobalt chalcogenides that have been theoretically predicted but heretofore never synthesized. Through topochemical means, we preserve the underlying layered structure by the kinetic removal (or insertion) of structural motifs from the thermodynamically stable phases.

In this study, we target topochemical deintercalation of extended solids with the stoichiometry $A_xM_2Ch_2$ where A = alkali metal, M = transition metal, and Ch is a chalcogenide that crystallize with the $ThCr_2Si_2$-type structure. The Inorganic Crystallographic Structural Database (ICSD) lists close to 1865 compounds with the $ThCr_2Si_2$-type structure, of which approximately 40 are chalcogenides. Just as perovskite-derived metal oxides have been utilized for topochemical conversion to metastable oxides,[5−8] $ThCr_2Si_2$-derived chalcogenides (and pnictides) can be the basis for new metastable nonoxides. Greenblatt et al. have already developed effective and straightforward methods to synthesize a variety of ternary or quaternary chalcogenides with this structure type.[9−11] Recently, we have demonstrated that *chemie douce* methods can be applied to such structures to produce iron-based superconductors such as FeS,[12] $(Li_{1-x}Fe_xOH)FeSe$,[13] $[Na_{1-x}Fe_x(OH)_2]FeS$, and $(Li_{1-x}Fe_xOH)FeS$.[14]

Until now, iron has been found to be the only transition metal to form stable binary chalcogenides with the anti-PbO type structure. In compounds such as tetragonal mackinawite FeS and β-FeSe, the $FeCh_4$ tetrahedra edge-share to form two-dimensional (2D) layers held by weak van der Waals interactions. Therefore, in addition to superconductivity, another appealing feature of the layered chalcogenides is their ability to act as hosts for intercalation chemistry.[15] In the FeSe case, its T_c can be increased from 8 K[3] to ≈43 K by intercalating either cationic species[16,17] or layers such as $(Li_{1-x}Fe_xOH)$.[18,19] Therefore, we have decided to test our topochemical method by focusing on cobalt in order to also help answer the question of what makes iron so special for superconductivity in these layered materials.

Received: October 3, 2016
Published: November 29, 2016

DOI: 10.1021/jacs.6b10229
J. Am. Chem. Soc. 2016, 138, 16432−16442

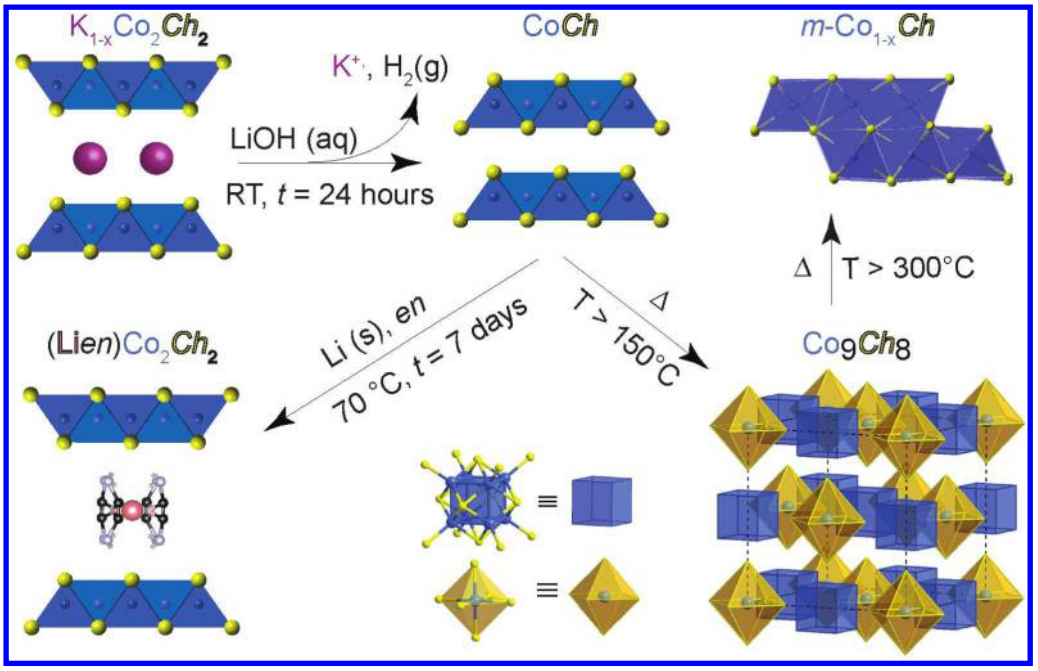

Figure 1. Reaction schemes for the manipulation of cobalt chalcogenides. From the thermodynamically stable $K_xCo_2Ch_2$ phases, we prepare metastable tetragonal Co*Ch* and (Li*en*)Co*Ch* where *en* = ethylenediamine. Upon applying heat to the mestable phases, pentlandite (Co_9Se_8) is prepared followed by the NiAs-derivative m-$Co_{1-x}Ch$.

First, we highlight the deintercalation reaction of Figure 1 to synthesize the hypothesized metastable tetragonal CoS and CoSe phases. Then, we will demonstrate how these new tetragonal phases, much as in the layered Fe*Ch* compounds, can serve as hosts for intercalation chemistry by using Li-ethylenediamine (Li-*en*) as a guest species (Figure 1). We characterize the physical properties of these metastable phases and demonstrate that changing the symmetry, metal oxidation state, and electronic configuration have a profound effect on the physical properties of these materials. Similarly, Shatruk and co-workers have reported drastic change of magnetic ordering of Co sublattice by electron doping for the $ThCr_2Si_2$-type layered rare-earth (R) cobalt pnictides (Pn), RCo_2Pn_2.[20−24] Finally, we use ab initio calculations to explain why the topochemical approach is necessary and successful for the preparation of Co*Ch* phases. We find that the application of bonding analysis[25,26] to our solid state structures not only aids the interpretation of the first-principles calculations, but also improves our predictive capability for finding new functional materials.

EXPERIMENTAL SECTION

Sample Synthesis. Binary anti-PbO type CoSe and CoS single crystals and powders were prepared by deintercalation of interlayer potassium cations from KCo_2Se_2 and KCo_2S_2 by a topochemical approach. For the synthesis of KCo_2Se_2 (or KCo_2S_2), 1:1 stoichiometric ratios of hexagonal CoSe (or CoS) were mixed with potassium metal (Sigma-Aldrich 99.5%) and loaded into a quartz ampule inside an argon-filled glovebox. The mixture was sealed using a double-ampule technique, a bigger ampule enclosing a smaller ampule containing the mixture, to avoid oxidation, and heated to 1050 °C at a rate of 10 °C/hour and held at this temperature for 5 h to form a congruent melt. Afterward, the melt was slowly cooled at a rate of 5 °C/hour to 450 °C to allow for crystal growth. Upon recovery, KCo_2Se_2 appeared as golden plate-like crystals and KCo_2S_2 golden polycrystalline material.

Two methods were employed to yield the tetragonal CoSe and CoS. First, KCo_2Se_2 or KCo_2S_2, crystals or powders respectively, were placed into ∼10 mL of saturated LiOH solution, made by dissolving $LiOH{\cdot}H_2O$ (Alfa Aesar 98%) in water. The mixtures were then placed in a vial for ultrasonication in a water bath for approximately 1 h. After 1 h, the contents were centrifuged and washed thrice to yield black powders. Another method was employed for the KCo_2Se_2 single crystals without the use of ultrasonication to avoid excessive break up of the crystallites. KCo_2Se_2 single crystals were added to ∼20 mL of saturated LiOH or ammonia solution in a flask, placed on a Schlenk line under argon gas and stirred for approximately 1 day. Shiny silver flaky crystals were recovered, washed and dried under vacuum. The highly basic solutions during the deintercalation reactions stabilize Se^{2-} anions over the formation of H_2Se and HSe^- species in solution, and subsequently prevented dissolution of the selenide layers. The deintercalation reaction dynamics as a function of pH are discussed in more detail in our earlier work.[13]

Characterization Methods. Powder X-ray diffraction (PXRD) data was collected using a Bruker D8 X-ray diffractometer with Cu Kα radiation, λ = 1.5406 Å (step size = 0.020°). Low temperature (3 K) diffraction data for CoSe were collected on the BT-1 high-resolution neutron powder diffraction (NPD) with the Ge(311) monochromator (λ = 2.0790 Å) at the NIST Center for Neutron Research. Temperature dependent PXRD on ground crystals of CoSe was performed using a Bruker C2 diffractometer with a Vantec500 2D detector, λ = 1.5406 Å (step size = 0.015°, 2θ = 13.5°−74°). The sample was heated using an Anton Paar DHS 1100 graphite-dome stage with heating from 27 to 600 °C under Ar flow to determine stability of the tetragonal CoSe phase. Rietveld and Pawley refinements with all the diffraction data were carried out using the TOPAS 4.2 software.[27]

Elemental analysis was performed using scanning electron microscopy (SEM) on a Hitachi SU-70 Schottky field emission gun SEM with an equipped Bruker Quantax energy dispersive X-ray detector. Energy dispersive X-ray spectroscopy (EDS) was carried out at 15 keV. Inductively coupled plasma atomic emission spectroscopy (ICP-AES) data were collected using an Shimadzu ICPE-9000 spectrometer. Standards used for ICP-AES were diluted from 1000 ppm of respective elements purchased from Fluka.

All magnetic susceptibility measurements were carried out using a Quantum Design Magnetic Susceptibility Measurement System (MPMS)[60] on powder samples of KCo_2Se_2, KCo_2S_2, and tetragonal

DOI: 10.1021/jacs.6b10229
J. Am. Chem. Soc. 2016, 138, 16432−16442

CoSe and CoS. Field-cooled (FC) and zero field-cooled measurements (ZFC) were taken from 1.8 to 300 K with various applied magnetic fields. Magnetic hysteresis measurements were taken at a series of temperatures, (1.8, 60, and 120 K) with applied magnetic field between $H = \pm 7$ T.

Electrical transport measurements were performed using a 9 T Quantum Design Physical Property Measurement System (PPMS-9). Single crystals of CoSe were mounted on a Quantum Design DC resistivity puck. Thin gold wires were attached to the crystal to form electrical contacts via silver paste. An applied current of 0.1 mA with frequencies near 10 Hz was utilized.

Computational Methods. All density functional theory (DFT)[28,29] calculations were performed by using the Vienna Ab-initio Simulation Package (VASP)[30−33] software package with potentials using the projector augmented wave (PAW)[34] method. The exchange and correlation functional were treated by the generalized gradient approximation (PBE-GGA).[35] The cutoff energy, 450 eV, was applied to the valence electronic wave functions expanded in a plane-wave basis set for all chalcogenides. A Monkhorst−Pack[36] generated 23 × 23 × 17 k-point grid was used for the Brillouin-zone integration to obtain accurate electronic structures. Crystal orbital Hamilton populations (COHP) were extracted using the program Local-Orbital Basis Suite Toward Electronic-Structure Reconstruction (LOBSTER) developed by Dronskowski et al.[37−40] COHP provides an intuitive chemical bonding analysis to the calculated electronic structures.

RESULTS

Topochemical Deintercalation. As illustrated in Figure 1, the topochemical deintercalation process leading to anti-PbO type Co*Ch* (**2**) is traced in the reaction from **1** to **2**. In this process, KCo_2Ch_2 reacts with water to form H_2 gas and KOH, and this reaction is depicted below.

$$KCo_2Ch_2(s) + H_2O(l) \rightarrow 2CoCh(s) + KOH(aq) + \frac{1}{2}H_2(g) \quad (1)$$

The reaction for the kinetic study was carried out in water without LiOH. During the deintercalation of the sample in water, we observed the evolution of gas bubbles, which are more rigorous when ultrasonication is applied. When the deintercalation was complete, the pH of the filtered solution was highly basic, suggesting the formation of KOH by the reduction of water.

The evolution of the hydrogen gas allowed us to study the reaction rate for the formation of the metastable Co*Ch* phases. A semiquantitative experiment measuring the volume of hydrogen gas evolved was set up by connecting two Erlenmeyer flasks—one as the reaction flask and the other as the H_2 measurement flask (Figure S1). The two flasks were tightly sealed, so that hydrogen generated in the reaction flask could only flow into the capturing flask, which expelled an equal volume amount of water. The expelled water was collected in a graduated cylinder via a cannula and measured as a function of time.

From eq 1 we express the reaction rate as $r = d[KOH]/dt = 2[H_2]/dt$. Approximating the molar volume of H_2 gas with that of an ideal gas, we can then relate the value of molar concentration [KOH] generated to the volume of expelled water.

$$n_{KOH} = \frac{2V_{H2}}{22.4\ \text{L mol}^{-1}} \quad (2)$$

$$[KOH] = \frac{V_{H2O}}{V_{sol} \times 11.2\ \text{L mol}^{-1}} \quad (3)$$

where V_{H2} and V_{H2O} are volumes of hydrogen gas generated and water expelled, respectively, V_{sol} the volume of the deintercalation solution, and n_{KOH} is the number of moles of KOH. Since the reactants include an insoluble solid and the solvent (i.e., water), then a plausible rate law could be written in terms of the molar concentration of the products $[H_2]$ or [KOH]. The amount of water expelled was observed to have a $t^{1/2}$ behavior as shown in Figure 2, which would be consistent with a rate law that has the form $r = k/[KOH]$. For a derivation of this proposed rate law from the $t^{1/2}$ dependence, see Supporting Information.

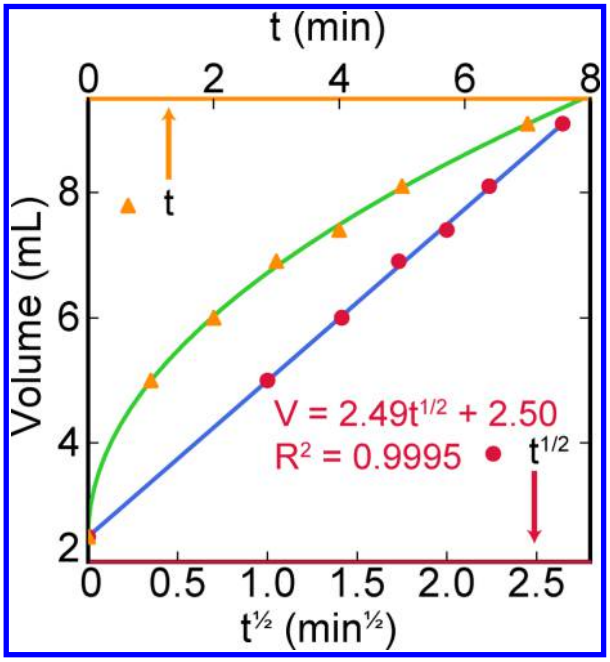

Figure 2. Volume of hydrogen generated during a deintercalation reaction of KCo_2Se_2 vs time t and $t^{1/2}$ leading to the preparation of pure CoSe. For this reaction, $t = 0$ is the point when water flow was observed from H_2 generation. The lines drawn represent a least-square fit of the data.

The results from the semiquantitative analysis of the reaction kinetics confirm that the deintercalation of KCo_2Se_2 involves the hydration of K^+ cations and the transfer of electrons between $Co^{1.5+}$ centers and H_2O molecules to evolve H_2 gas and OH^- groups. We postulate that the deintercalation reaction is in part driven by the oxidation of $Co^{1.5+}$, and since the reaction conditions are mildly oxidative at room temperature, no major structural reconstruction of the chalcogenides occurs. Therefore, the sheets of edge-sharing $CoCh_4$ tetrahedra in KCo_2Ch_2 are retained, but the layers does undergo a rearrangement from the body-centered to the primitive setting. Overall, kinetically controlled topochemical deintercalation leads to the first isolation of anti-PbO type CoSe and CoS.

Crystallography, Chemical Composition, and Thermal Stability. Comparisons of the PXRD patterns of ground single crystals of KCo_2Se_2 and CoSe are shown in Figure 3, and the NPD results are shown in Figure 3c. PXRD patterns of the sulfide analogues are shown in Figure 4. As seen from both the X-ray and neutron data, the crystal structures of both

DOI: 10.1021/jacs.6b10229
J. Am. Chem. Soc. 2016, 138, 16432−16442

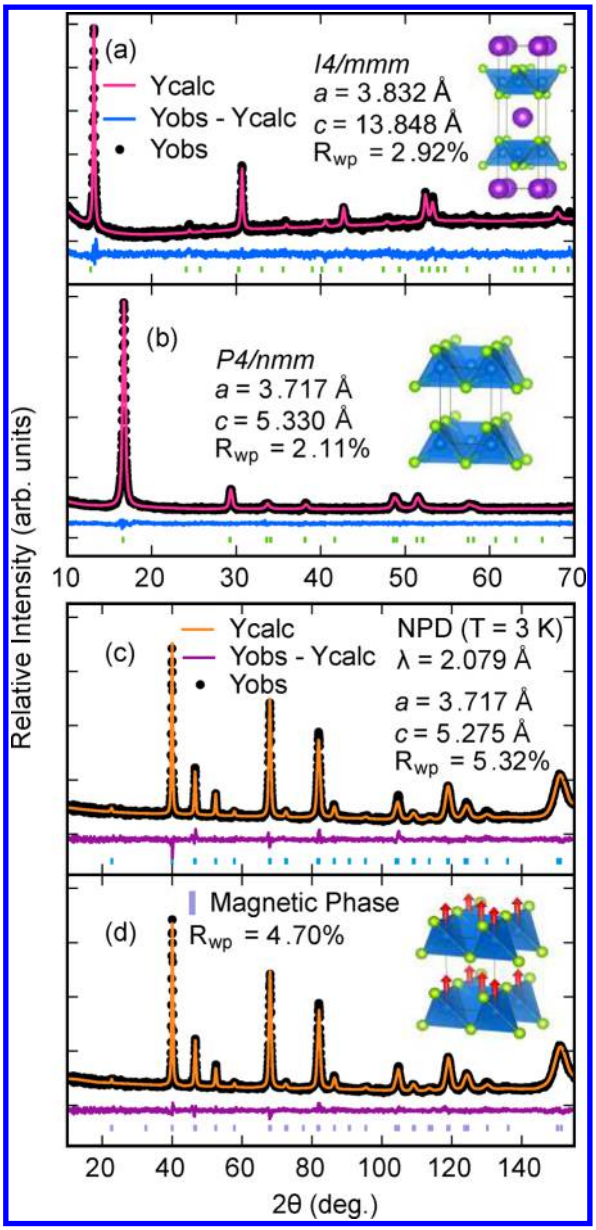

Figure 3. Powder X-ray diffraction patterns with Cu Kα radiation of (a) KCo_2Se_2 in the body-centered tetragonal structure ($I4/mmm$) at room temperature and (b) CoSe with a primitive tetragonal structure ($P4/nmm$) at room temperature. (c) Neutron powder diffraction (NPD) pattern of CoSe at 3 K (BT-1, NIST). (d) The NPD pattern but with the addition of the ferromagnetic phase with the moment on the Co site pointing in the c-direction as shown in the inset. Tick marks representing the corresponding tetragonal phases are shown below the calculated, observed, and differences curves from Rietveld analysis.

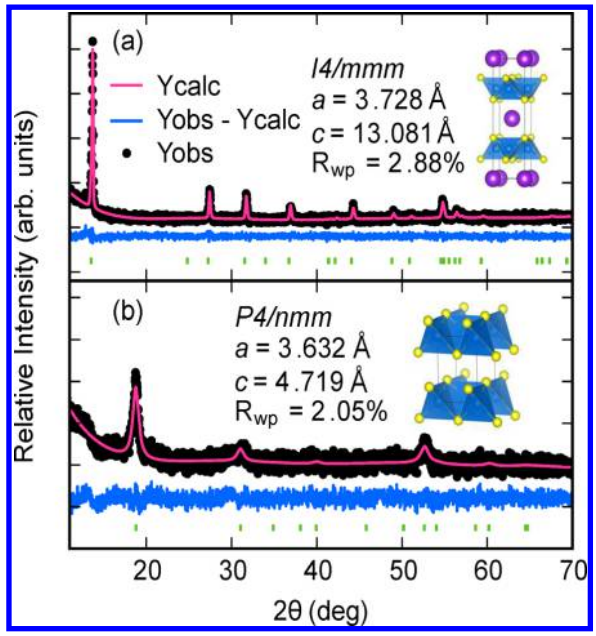

Figure 4. Powder X-ray diffraction patterns with Cu Kα radiation of (a) KCo_2S_2 and (b) CoS collected at room temperature. Tick marks representing the corresponding tetragonal phases are shown below the calculated, observed, and differences curves from Rietveld analysis for (a) and Pawley fit for (b).

deintercalated CoSe and CoS can be fit well with the anti-PbO type structure, which has the primitive space group $P4/nmm$. Detailed structural information extracted by Rietveld refinements of PXRD and NPD for the selenides and sulfides are reported in Table 1 and Table S2, respectively.

Elemental analysis from EDS gave a Co:Se ratio close to 0.94:1 (Table S3), but the more accurate ICP-AES measurement gave a composition of $Co_{0.98\pm0.02}Se$. Therefore, while it is likely that the starting compositions of KCo_2Se_2 could have some vacancies on the cobalt site, our resulting CoSe products show little evidence for significant vacancies on the Co site. Furthermore, for CoSe no residual potassium could be detected by EDS, suggesting complete deintercalation. For CoS, however, about 4.5 at% of potassium was measured by EDS (Table S3). While the residual potassium in CoS could be further reduced by longer reaction time with ultrasound, this usually resulted in worse crystallinity in the products.

Although CoSe and CoS have been prepared for the first time in their tetragonal form, the sulfide appears to be less stable than the selenide. In addition to its poor crystallinity (Figure 4), certain ($hk0$) reflections are missing for CoS, which indicates some disorder within its ab plane. For longer deintercalation reactions, up to 5 h under ultrasonication, the as-recovered CoS sample was amorphous as no Bragg reflection could be identified. Contrastingly, prolonged reactions for CoSe samples led to no noticeable changes in its crystallinity. Our results suggest that anti-PbO type CoS can be stabilized kinetically, but it is much less stable than the selenide analogue.

In order to exploit tetragonal CoSe as an intercalation host, temperature dependent PXRD was carried out to examine its thermal stability. Powders of ground single crystals of CoSe were heated from 27 to 600 °C, and the evolution of the PXRD patterns is shown in Figure S4. Upon heating to 200 °C, the tetragonal CoSe ($P4/nmm$) completely transformed to cubic cobalt seleno-pentlandite (Co_9Se_8, $F\bar{4}3m$, Figure 1). Around 400 °C, the cubic Co_9Se_8 phase started to convert to a monoclinic phase (Co_3Se_4, $C2/m$), a distorted and vacancy-ordered NiAs-type (Figure 1). This monoclinic phase persisted to 600 °C and remained the major phase when cooled back to room temperature.

The results between 200 and 600 °C are in good agreement with the phase diagram of the Co−Se system.[41] The transformation from tetragonal CoSe to the Co_9Se_8 pentlandite structure between 150 and 200 °C suggests that any intercalation reactions of the anti-PbO type CoSe need to be

DOI: 10.1021/jacs.6b10229
J. Am. Chem. Soc. 2016, 138, 16432−16442

Table 1. Structural Parameters for Ground Single Crystals of KCo_2Se_2 and CoSe[a]

KCo_2Se_2 (298 K, PXRD), $I4/mmm$, R_{wp} = 2.917%						
a = 3.832(2) Å, c = 13.848(3) Å						
atom	site	x	y	z	occ.	U_{iso} (Å^2)
K1	2a	0	0	0	0.94(6)	0.109(22)
Co1	4d	0	0.5	0.25	0.96(6)	0.060(11)
Se1	4e	0	0	0.359(3)	1	0.019(4)
Co−Se (Å)	Se−Co−Se (deg)	Se−Co−Se (deg)	Co−Co (Å)	anion height (Å)		
2.442(6)	103.4(4)	112.6(2)	2.710(3)	1.509(3)		
CoSe (298 K, PXRD), $P4/nmm$, R_{wp} = 2.102%						
a = 3.717(3) Å, c = 5.330(3) Å						
atom	site	x	y	z	occ.	U_{iso} (Å^2)
Co1	2a	0	0	0	1	0.012(3)
Se1	2c	0	0.5	0.265(5)	1	0.010(3)
Co−Se (Å)	Se−Co−Se (deg)	Se−Co−Se(deg)	Co−Co (Å)	anion height (Å)		
2.332(2)	111.382(63)	105.8(2)	2.6284(3)	1.412(3)		
CoSe (3 K, NPD), $P4/nmm$, R_{wp} = 5.318%						
a = 3.716(6) Å, c = 5.275(1) Å						
atom	site	x	y	z	occ.	U_{iso} (Å^2)
Co1	2a	0	0	0	1	0.0026(8)
Se1	2c	0	0.5	0.269(2)	1	0.0020(5)
Co−Se (Å)	Se−Co−Se (deg)	Se−Co−Se(deg)	Co−Co (Å)	anion height (Å)		
2.339(5)	111.632(36)	105.232(68)	2.6280	1.412(3)		

[a]Structures are for room temperature PXRD data and 3 K NPD data. All relevant bond angles and distances from the refinements are given. Standard uncertainties given in parentheses indicate one standard deviation.

limited to below 200 °C in order to avoid structural reconstruction of the selenide sublattice.

Although pentlandite-type Co_9Se_8 exists on the Co−Se phase diagram below 400 °C, it is unusual to prepare it by direct phase transformation as it has very limited window of phase stability.[41] For an approximately 1:1 Co/Se ratio, the NiAs type variant is favored thermodynamically from room temperature to about 1100 °C. In fact, octahedral coordination of Co^{2+} in selenides dominates most regions of the phase diagram as in the NiAs and pyrite-type structures. Therefore, predominately tetrahedrally coordinated cobalt in pentlandite can only be formed by annealing samples at 400 °C within a narrow compositional window.[42] It is likely that the transformation from anti-PbO type CoSe to pentlandite is kinetically favored since it does not require overcoming the high energy barrier associated with changing coordination geometry of cobalt. Therefore, the monoclinic phase exists as a thermodynamic sink, and once formed, it does not revert back to the pentlandite structure when cooling from 600 °C to room temperature.

Magnetic Properties. Upon deintercalation of potassium from KCo_2Se_2 to form CoSe, a drastic change was observed in their respective magnetic properties (Figure 5). KCo_2S_2 displays temperature independent magnetic susceptibility above 85 K indicative of Pauli paramagnetism. Below, 85 K, the magnetization diverges and appears to be ferromagnetic with a Curie temperature (T_C) near 82 K. For completely deintercalated CoSe, its T_C decreased to about 10 K and its response to magnetic field became significantly weaker compared to KCo_2Se_2. The previous report by Yang et al. showed KCo_2Se_2 to have a T_C = 74 K,[43] which might indicate that the amount of potassium in the lattice, and hence the electron filling level, influences the magnetic properties.

To shed more light on this it is useful to briefly discuss the recent studies on RCo_2P_2 phases where R = rare earth. These isostructural cobalt phosphides are thought to display charge transfer from the rare-earth 4*f* shell to the Co 3*d* level, which alters the magnetic behavior of Co square sublattice.[20−22] In our selenide samples, the formal oxidation state of Co changes from approximately +1.5 in KCo_2Se_2 to +2 in CoSe. This indicates that charge transfer from the K cations effectively enhances ferromagnetism in the Co sublattice and raises its T_C. Furthermore, an increase in T_C has also been observed when the Co−Co distance in $La_{1-x}Pr_xCo_2P_2$ is increased.[20,44] We observe the same trend in the cobalt selenides as the Co−Co distance increases from 2.6284(3) Å in CoSe to 2.710(3) Å in KCo_2Se_2. Therefore, it seems plausible that the electronic structure responsible for ferromagnetism is heavily influenced by both the metal−metal distances in the square lattice and the transition metal's electron configuration.

The differences between KCo_2Se_2 and CoSe were further elaborated by their respective isothermal magnetization measurements (Figure 6). KCo_2Se_2 demonstrates clear hysteretic behavior indicative of the ferromagnetic ordering at low temperature. Similar to the work of Yang et al.,[43] we observe a small coercive field and complete saturation of the magnetization in KCo_2Se_2, approaching a value of 0.6 μ_B/Co, whereas for CoSe, no saturation was observed for a field up to 7 T. In addition, CoSe seems to carry a much smaller moment of ≈0.1 μ_B/Co at H = 7 T. The lack of complete saturation to the expected 3 μ_B for a tetrahedral Co^{2+} crystal field can be attributed to the itinerant character of ferromagnetism in these materials.[45] In comparison to the more complex magnetic phase diagram of the layered cobalt oxide system, Li_xCoO_2, the deinterclation of K^+ from KCo_2Se_2 mostly affects the T_C instead of the types of magnetic ordering (i.e., various antiferromagnetic phases).[46] We attribute this difference in the physical

DOI: 10.1021/jacs.6b10229
J. Am. Chem. Soc. 2016, 138, 16432−16442

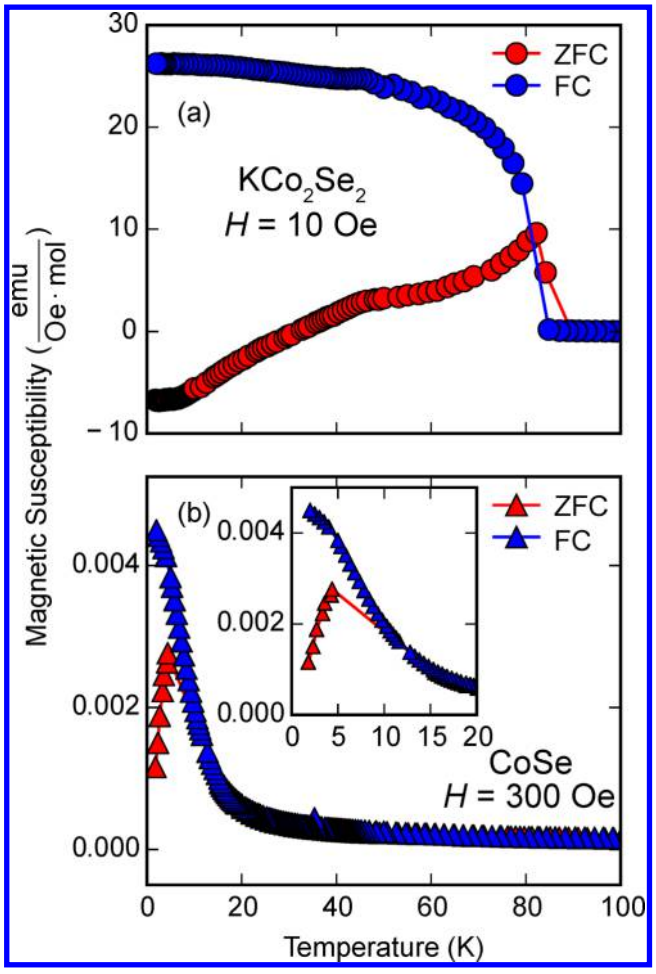

Figure 5. Magnetic susceptibility of (a) KCo_2Se_2 and (b) CoSe, vs temperature measured in applied field of 10 and 300 Oe, respectively. (a) KCo_2Se_2 displays a ferromagnetic transition at T_C = 82 K and (b) CoSe a T_C = 10 K; the inset shows zoomed-in region near T_C.

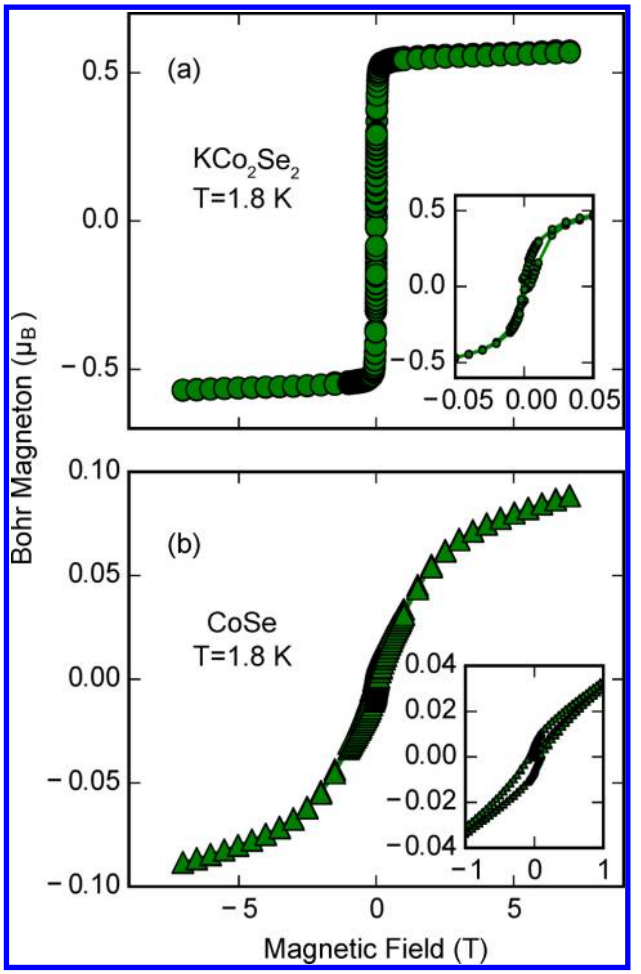

Figure 6. Isothermal magnetization vs applied field H for (a) KCo_2Se_2 and (b) CoSe at 1.8 K. Both KCo_2Se_2 and CoSe show hysteretic behavior indicating ferromagnetic ordering.

properties to the multiple structural transitions as a function of x in Li_xCoO_2 whereas we do not observe such transitions in the KCo_2Se_2 system.

CoSe shows clear ferromagnetic hysteresis at 1.8 K (Figure 6), and in order to confirm the validity of this ferromagnetic signal, isothermal magnetization for CoSe was performed at various temperatures: 2, 60, and 150 K (Figure 7). With the increase of temperature to 60 K, the hysteretic behavior for CoSe disappears and paramagnetic behavior emerges. In addition, the paramagnetic behavior at 60 K indicates the absence of any residual KCo_2Se_2 in the sample since 60 K is well below its Curie temperature.

CoS shows similar magnetic behavior to CoSe (Figure S5). A ferromagnetic transition around 10 K was observed for CoS, and hysteretic behavior at 1.8 K that does not fully saturate at applied fields up to ±7 T. A more thorough magnetic study may be required to elucidate the sublte differences between the selenides and sulfides. Such a study would be useful in light of the fact that the iron analogues, FeSe and FeS, display a differet superconducting critical temperatures, 8 and 5 K, respectively.

Neutron diffraction remains one of the most powerful tools for elucidating the long-range magnetic ordering in materials, and our NPD data further elucidates the nature of such ordering in CoSe. First, the NPD does not indicate any long-range antiferromagnetic ordering in CoSe since the 3 K pattern (Figure 3c) does not display any satellite reflections. We therefore rule out ferrimagnetic ordering as the cause of the hysteresis in the magnetization data. Second, we fit a ferromagnetic phase to the NPD data (Figure 3d) and obtain a moment of 0.30(17) μ_B pointing only in the c-direction. After considering the magnetic contributions to the nuclear phase, the R_{wp} of the refinement decreased from 5.3% to 4.7%, indicating meaningful improvement of the statistics. The value for the moment may not be conclusive; however, due to the limitations of unpolarized neutron diffraction, where it is impossible to separate the nuclear from the magnetic contributions to the Bragg reflections. It is important to note that our attempt to refine the magnetic moment for the 15 K NPD data led to a divergence in the fit. Since the moment is apparently small from the magnetization data, more careful temperature-dependent neutron diffraction studies may be carried out on a single crystal to study the nature of the weak itinerant ferromagnetism in CoSe.

Electrical Resistivity. Temperature dependent electrical resistivity of CoSe single crystal is presented in Figure 8. The resistivity displays typical metallic behavior down to approximately 10 K, the proposed Curie temperature for CoSe. Due to the lack of single crystal KCo_2S_2, a single crystal of CoS was not prepared and no transport data is presented for CoS.

The properties of CoSe can be summarized as a weak ferromagnetic metal. In the region below 10 K, (Figure 8 inset),

DOI: 10.1021/jacs.6b10229
J. Am. Chem. Soc. 2016, 138, 16432−16442

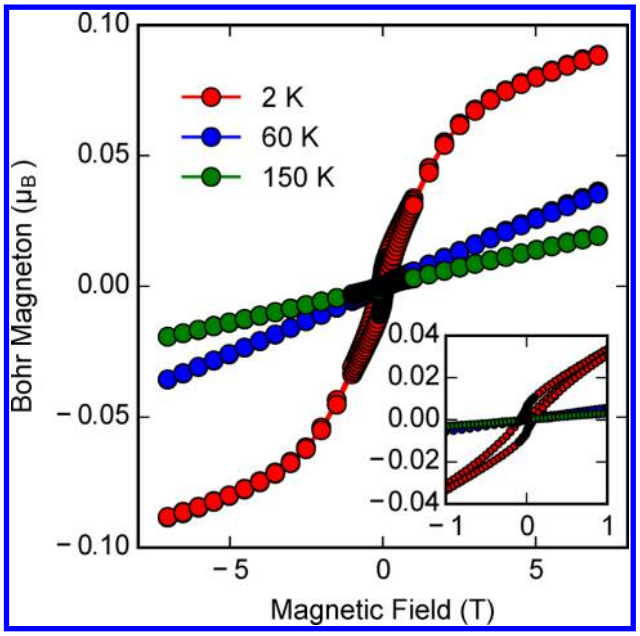

Figure 7. Isothermal magnetization vs applied field H for CoSe at T = 2, 60, and 150 K. While the 2 K data displays hysteresis with some blocking, the 60 and 150 K data indicate paramagnetic behavior. The inset shows a zoomed region emphasizing the disappearance of hysteresis at higher temperatures.

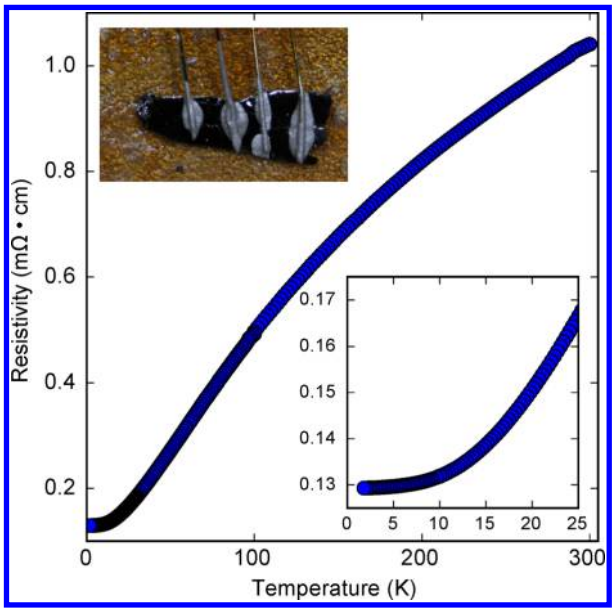

Figure 8. Temperature dependent electrical resistivity of CoSe measured on a single crystal. CoSe displays metallic behavior at high temperature with a slight deviation in slope around 10 K (inset), close to the ferromagnetic transition temperature.

the slope of the resistivity curve changes abruptly from the high temperature region. This change is indicative of the ferromagnetic transition occurring at 10 K. It is known that ferromagnetic materials display clear T^2 behavior at low temperature, below T_C, due to electron−electron scattering[47] and typical Fermi liquid behavior. This behavior is more profound in the ferromagnetic parent KCo_2Se_2 compound (Figure S11). Its temperature-dependent resistivity clearly shows linear correlation above 80 K close to its T_C (74 K), and T^2 behavior below 80 K. With the addition of spin fluctuations contributions, electrical resistivity of a weak ferromagnet is predicted to have significant $T^{5/3}$ behavior near the transition temperature.[48] The low temperature resistivity of CoSe does not display clear $T^{5/3}$ or T^2 behavior, and is likely a combination of the two. This can be attributed to the very low Curie temperature of CoSe; there is no distinct range for which different scattering processes will dominate, causing the overlap in temperature dependencies.

DISCUSSION

Deintercalation Chemistry of Late Transition Metal Chalcogenides. It is interesting to consider the crystallographic changes induced by our topochemical method for deintercalation of AM_2Ch_2-type phases, and compare it with others recently published in the literature.[49] Depending on the synthetic conditions and the chemical system, kinetically controlled deintercalation can also induce structural reconfiguration. In our topochemical deintercalation, only a shift in the stacking of the alternating planes of Co*Ch* along the *c*-direction occurs. As the deintercalation proceeds, the body-centered operation is lost while an *n*-glide plane is introduced to change the Co*Ch* stacking sequence (Figure 1). Otherwise, no major reconstruction occurs within the Co*Ch* planes, and the transition metal, whether iron or cobalt, remains in tetrahedral geometry.

So far we have demonstrated success on preparing anti-PbO type Fe and Co chalcogenides via our topochemical deintercalation approach. Despite similar strategies, their respective synthetic conditions are not mutually interchangeable. As reported in our earlier work on single crystal tetragonal FeS obtained by deintercalation of KFe_2S_2,[12] highly basic hydrothermal conditions are oxidative and can lead to large concentrations of Fe vacancies. Hydrothermally prepared FeSe can also lead to a large number of vacancies, which are detrimental to superconductivity.[50] To remedy this, extra Fe powder was added in the autoclave to create a reducing environment and fill the Fe vacancies. The differences between the preparations of Fe*Ch* and Co*Ch* suggest that fine-tuning of synthetic conditions will be required to obtain other anti-PbO type transition metal chalcogenides.

In all, it must be said that the target of other anti-PbO type *MCh* systems may be significantly harder to achieve in comparison to the cobalt analogues. A recent comprehensive study on the deintercalation reaction conditions of KNi_2Se_2 reported by Neilson and McQueen[49] sheds more light on this. Utilizing stronger oxidization conditions produced by CuI_2 in acetonitrile, they reported formation of NiAs-type hexagonal NiSe from the $ThCr_2Si_2$-type KNi_2Se_2. Accompanying the deintercalation of K^+, edge-sharing layered $NiSe_4$ tetrahedra in KNi_2Se_2 completely transform to corner-sharing $NiSe_6$ octahedra. Although, this deintercalation reaction is kinetically controlled, upon losing too much K^+, KNi_2Se_2 does not retain the original tetrahedral layered structure and transforms directly to the thermodynamically stable hexagonal NiSe. One of the major discoveries for this deintercalation process is that the increase of Ni vacancies and Ni oxidation are the driving forces for structural reconstruction.[49]

Intercalation Chemistry of Late Transition Metal Chalcogenides. Ever since Gamble et al. prepared a large new family of intercalated layered transition metal dichalcogenides in the early 1970s to explore superconductivity,[51,52] intercalation chemistry has remained a great tool for the manipulation of layered materials held by van der Waals

DOI: 10.1021/jacs.6b10229
J. Am. Chem. Soc. 2016, 138, 16432−16442

interactions. Intercalation chemistry via *chimie douce* methods in iron-based superconductors has more recently been pioneered by Clarke et al.[16,53] to overcome the common impurity phases that form from solid-state reactions of alkali metals with iron chalcogenides.[54] Before now, one of the outstanding issues was that the thermodynamically available tetragonal chalcogenides were limited to iron. With the discovery of the anti-PbO type Co*Ch* in the present study, we now have the opportunity to explore intercalation chemistry in this new family.

First, we present the ion exchange reaction of KCo_2Se_2 single crystals with LiOH using a similar hydrothermal route for LiOH intercalated FeSe from our previous work.[13] Hydrothermal reactions using LiOH, selenourea, and H_2O along with single crystals of KCo_2Se_2 reacted at 100−160 °C for 1−3 days. Reactions at 100−120 °C yielded a mixture of the tetragonal CoSe and the pentlandite type Co_9Se_8, while reactions at 140 °C and above gave pure seleno-pentlandite in single crystal form (Figure S6, Table S4). Although attempts to synthesize (LiOH)CoSe were not successful, our method provides a route to high purity single crystal seleno-pentlandite, which was not available previously.

After the lack of success with LiOH intercalation, we present the direct intercalation with amine adducts of Li metal. The smaller layer spacing in the CoSe compared to the iron analogue (5.33 Å in CoSe vs 5.52 Å in FeSe) could be an impediment to intercalation, so we used ethlyenediamine (*en*) instead of liquid ammonia as the solvent to perform the reaction at an elevated temperature. Tetragonal CoSe was reacted with Li metal dissolved in 15 mL *en* on a Schlenk line under Ar flow at 70−90 °C for 7 days. The PXRD pattern of the as-recovered product (Figure 9) closely matches the pattern

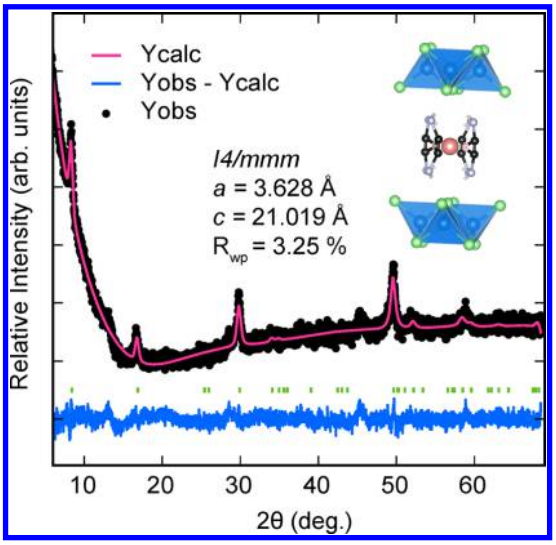

Figure 9. Powder X-ray diffraction patterns of ground polycrystalline $Li(C_2H_8N_2)CoSe$ collected at room temperature. Refinement of the $Li(C_2H_8N_2)CoSe$ structure in the body-centered tetragonal group (*I*4/*mmm*). Tick marks represent the corresponding phase.

of Li-*en* intercalated FeSe (Li-*en*-FeSe) reported by Hatakedra et al.[17] The new phase was fit to a body-centered tetragonal cell (*I*4/*mmm*) using the Pawley method, and its lattice constant *c* increased to 21.019 Å, which is comparable to Li-*en*-FeSe (20.74 Å[17]).

Although it is not possible to solve the structure of the Li-*en*-CoSe phase using our current PXRD data, a recent neutron diffraction study on Na-*en*-FeSe shed light on the structure of such amine-intercalated phases.[55] Using the model by Jin et al., the proposed structure for Li-*en*-CoSe is shown in Figure 9. To confirm the intercalation of Li cations into CoSe, the sample was heated to 800 °C in air to decompose it. The PXRD pattern of the decomposition product was fit well with the layered $LiCoO_2$ structure ($\bar{R}3m$), suggesting the presence of Li in the intercalated compound. The exciting implication of this result is that the intercalation chemistry for the Fe family can also be applied to the Co system.

First-principles calculations of the electronic density of states, and bonding analysis of such states may also provide answers as to the optimal electron filling level and the possible limits of topochemical deintercalation and intercalation. We discuss those in the next section.

Relationship to FeSe and DFT Predicted Stability. Anti-PbO type FeSe and FeS with critical temperatures (T_c's) of 8 K[3] and 4 K[4] respectively, are of great interest to the superconductivity community. The synthesis of the isostructural CoSe and CoS offers another point for investigation how the variation of electronic structure leads to superconductivity. Some basic physical and chemical properties of CoSe and CoS can be understood when analyzing the density of states (DOS) and their projected crystal orbital Hamilton population (pCOHP) of the cobalt system in comparison to the iron analogues. In particular, phase stability can be compared intuitively by analyzing their bonding and antibonding interactions using COHP extracted by the LOBSTER package provided by Dronskowski and co-workers.[37−40] The results of DFT calculations on CoSe and FeSe are shown in Figure 10.

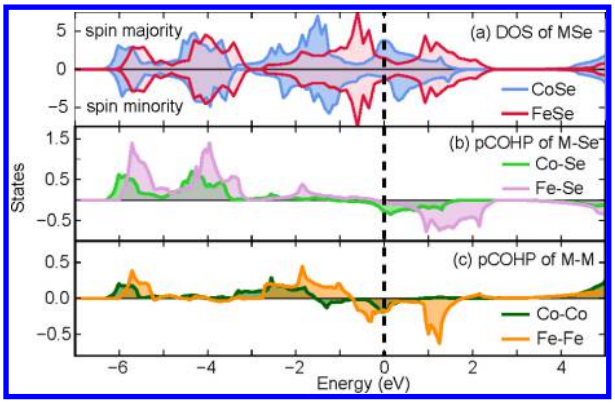

Figure 10. (a) The spin-polarized electronic density of states (DOS) of FeSe and CoSe. (b) The partial crystal orbital Hamilton population (pCOHP) to describe the *M*-Se bonding and antibonding intercations. (c) The pCOHP for *M*−*M* interactions. In (b) and (c), positive and negative states represent bonding and antibonding interactions, respectively.

In comparing the spin-polarized density of states (DOS) for CoSe with FeSe, the former shows clear splitting of the DOS near the Fermi level. This splitting matches Stoner's criterion for ferromagnetism, whereby the spin-polarized DOS are lowered in energy due to exchange interactions.[56] Similar exchange splitting is also observed for CoS (Figure S7). The predicted ground state magnetic moments on each Co atom in CoSe and CoS are 0.32 μ_B and 0.42 μ_B, respectively. Our DFT calculations therefore suggest weak itinerant ferromagnetism in

DOI: 10.1021/jacs.6b10229
J. Am. Chem. Soc. 2016, 138, 16432−16442

both tetragonal CoSe and CoS and well describe the physical property and neutron diffraction measurements. A previous DFT study by Ding et al.[57] did not predict CoSe to be ferromagnetic as spin-polarized calculations were not carried out.

To explore how the electronic structure affects phase stability, and hence the success of topochemical deintercalation, COHP analysis was performed for tetragonal Fe, Co and Ni chalcogenides (Figure 10, Figure S7 and Figure S8). Among this group, the anti-PbO type FeSe is the only thermodynamically stable one. The so-called β-FeSe is on the Fe−Se phase diagram and can be formed by direct reaction of the elements at high temperatures. In contrast, FeS, CoSe and CoS can only be synthesized using kinetically controlled and therefore low-temperature routes, and tetragonal NiSe and NiS remain hypothesized compounds.

COHP plots show that for *M*−*Ch* interactions, there are nearly negligible antibonding states at the Fermi-level for FeSe, whereas FeS, CoSe, and CoS (Figure 10 and Figure S7) show population of antibonding states increasing in the order listed. The increased antibonding character suggests that FeS, CoSe to CoS become less stable, which matches the observations from our synthetic work. For NiSe and NiS, both COHP plots (Figure S8) show stronger antibonding characters for Ni−*Ch* interactions, which may also explain why they have yet to be reported. In addition, NiSe shows significantly increased Ni−Ni antibonding interactions. By retaining the metal square sublattice, the stronger Ni−Ni antibonding interactions will increase as the deintercalation of K^+ proceeds. Such unfavorable interactions would then be countered by the formation of a large amount of Ni vacancies or structural reconstruction altogether.

One of the most interesting features of the iron-based superconductors has been the control of superconducting properties through the manipulation of the Fermi surface and therefore the filling of the electronic bands. Given the very similar tetragonal structures, the electronic dispersion curves along high-symmetry points of the Co*Ch* phases are similar to those of the Fe*Ch* phases. As shown in the partial DOS diagram of Figure 11, the ten dispersion curves from −2 eV to +2 eV correspond to the predominately 10 *d*-orbitals of the two transition metals per unit cell. Therefore, in the simple anti-PbO type structure for transition metal chalcogenides, the physical properties are derived from the occupation of the predominantly *d*-bands.

Since Co has one more electron than Fe, the Fermi level of CoSe moves to higher energy levels with respect to the Fe analogues (Figure 11 and Figure S9). Consequently, the hole pockets at the Γ-point close to the Fermi level in Fe*Ch* superconductors are missing in the Co*Ch* phases (Figure 12). The electron pockets at the M-point become much deeper for Co*Ch*. Since nesting of the electron and hole pockets is considered to be key for the superconducting mechanism, we did not anticipate the pure Co*Ch* phases to be superconducting on this simple diagram. Recent ARPES studies on the FeSe/STO monolayer superconductors ($T_c \sim 100$ K)[58,59] have revealed the absence of hole pocket at the Γ-point, and it is suggested that the electron pocket at M-point could be more important. Hence, it might be possible to tune Co*Ch* toward superconductivity by reducing the electron density near the M-point via Fe substitution on the Co site or As/P substitution on the chalcogenide site.

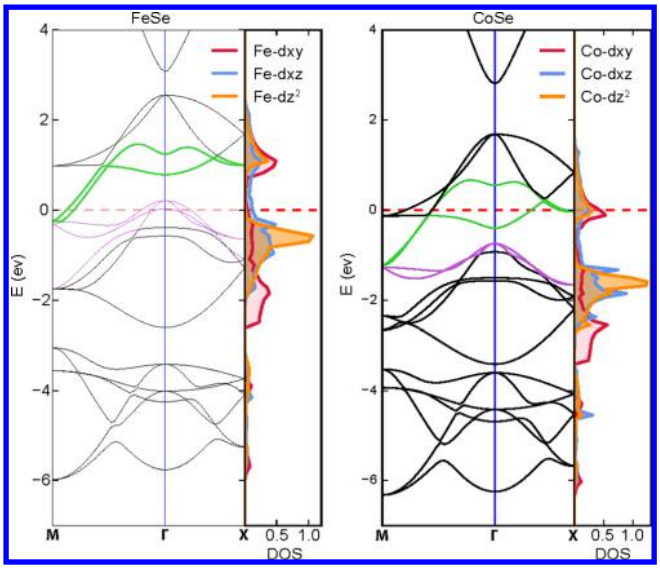

Figure 11. Band structure along three different directions and the corresponding partial DOS of 3*d* states for FeSe and CoSe. Purple and green lines in the band structure indicate bands crossing the Fermi-level close to the Γ and M points, respectively.

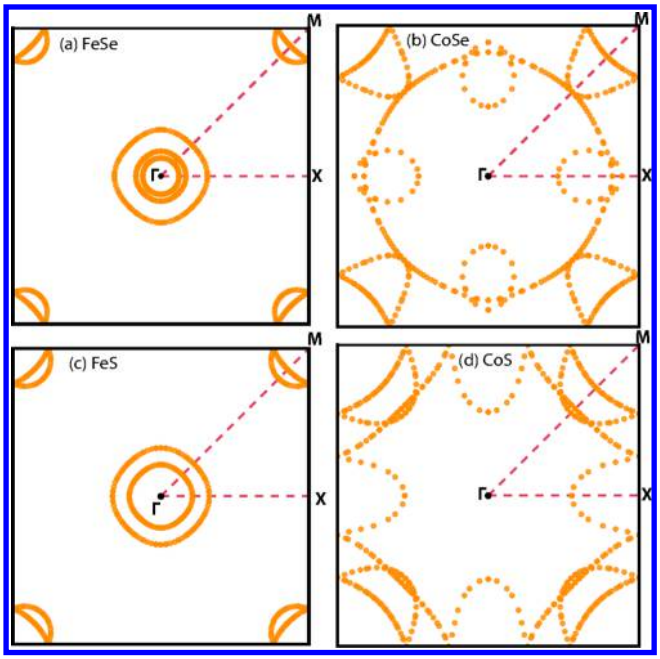

Figure 12. Fermi surface plots on the Γ−M−X plane for (a) FeSe, (b) CoSe, (c) FeS and (d) CoS.

The Fermi surfaces of Fe*Ch* are highly two-dimensional and manifest themselves as isolated 2D cylindrical sheet that do not overlap. As shown in their band structures (Figure 11a and Figure S9a), there are three bands crossing the Fermi level of FeSe close to the Γ-point, while there are only two for FeS. This is reflected on their Fermi surface plots, as three and two cylindrical sheets can be seen for FeSe and FeS, respectively. For Co*Ch*, because there is no hole pocket at the Γ-point, their Fermi surfaces have moved farther away from the Γ-point compared to Fe*Ch*. More importantly, a complete reconstruction of the Fermi surface occurs and in Co*Ch* a flatly dispersing band approaching the X-point is occupied.

DOI: 10.1021/jacs.6b10229
J. Am. Chem. Soc. 2016, 138, 16432−16442

CONCLUSIONS

We have demonstrated that through topochemical means, new binary phases can be prepared and particularly that kinetic control is a means to prepare novel 2D layered transition metal chalcogenides. These new phases can be stabilized if the topochemical deintercalation utilizes mild oxidative environment and replenishing metal vacancies in the chalcogenide layer. With this strategy we prepared the hypothesized metastable CoSe and CoS with the anti-PbO structure for the first time. These new Co*Ch* phases will now help answer some important questions regarding superconductivity in their iron analogues FeSe and FeS. Furthermore, the topochemical deintercalation of single crystalline KCo_2Se_2 lead the formation of single crystalline CoSe, which was key for more thorough exploration of physical properties such as electrical resistivity. Finally, our physical property and neutron diffraction measurements of CoSe reveals that it is a weak itinerant ferromagnet with a T_C near 10 K and a small moment near 0.1 μ_B per Co cation. Similar measurements for CoS reveal weak ferromagnetism as well, although the less crystalline nature of CoS impedes a more accurate determination of its physical properties.

DFT calculations support our interpretation of both CoSe and CoS as weak ferromagnetic metals, and the manner in which the Fermi level fills the predominately *d*-states helps explain why CoSe and CoS should not be expected to be superconductors. Furthermore, bonding analysis of the electronic DOS reveals that antibonding Co−*Ch* states are more occupied than in the case of the iron analogues, thus justifying the higher thermodynamic stability in the latter compounds.

Future work in this area includes further expansion of known layered *MCh* phases through intercalation chemistry. Our first attempts with bases such as Li-ethylenediamine indicate that CoSe can indeed act as intercalation host. Given that guest species can readily be inserted into these materials, we now have a tool to increase the two-dimensionality of the electronic structures. Since the simple electronic structure of the metal square sublattice does not seem to change much as a function of transition metal, we anticipate that the physical properties of new *MCh* phases could be predicted.

ASSOCIATED CONTENT

Supporting Information

The Supporting Information is available free of charge on the ACS Publications website at DOI: 10.1021/jacs.6b10229.

Crystal data (CIF)

Supporting tables, figures, and equations (PDF)

AUTHOR INFORMATION

Corresponding Author

*efrain@umd.edu

Notes

The authors declare no competing financial interest.

ACKNOWLEDGMENTS

Research at the University of Maryland was supported by the NSF Career DMR-1455118, the AFOSR Grant No. FA9550-14-10332, and the Gordon and Betty Moore Foundation Grant No. GBMF4419. We also acknowledge support from the Center for Nanophysics and Advanced Materials. The authors acknowledge the University of Maryland supercomputing resources (http://www.it.umd.edu/hpcc) made available for conducting the research reported in this paper. We acknowledge the support of the National Institute of Standards and Technology, U.S. Department of Commerce, in providing the neutron research facilities used in this work and the NIST awards 70NANB12H238 and 70NANB15H261.

REFERENCES

(1) de Pablo, J. J.; Jones, B.; Kovacs, C. L.; Ozolins, V.; Ramirez, A. P. *Curr. Opin. Solid State Mater. Sci.* **2014**, *18*, 99−117.

(2) Jain, A.; Persson, K. A.; Ceder, G. *APL Mater.* **2016**, *4*, 053102.

(3) Hsu, F.-C.; Luo, J.-Y.; Yeh, K.-W.; Chen, T.-K.; Huang, T.-W.; Wu, P. M.; Lee, Y.-C.; Huang, Y.-L.; Chu, Y.-Y.; Yan, D.-C.; Wu, M.-K. *Proc. Natl. Acad. Sci. U. S. A.* **2008**, *105*, 14262−14264.

(4) Lai, X.; Zhang, H.; Wang, Y.; Wang, X.; Zhang, X.; Lin, J.; Huang, F. *J. Am. Chem. Soc.* **2015**, *137*, 10148−10151.

(5) Schaak, R. E.; Mallouk, T. E. *Chem. Mater.* **2002**, *14*, 1455−1471.

(6) Tsujimoto, Y.; Tassel, C.; Hayashi, N.; Watanabe, T.; Kageyama, H.; Yoshimura, K.; Takano, M.; Ceretti, M.; Ritter, C.; Paulus, W. *Nature* **2007**, *450*, 1062−1065.

(7) Tassel, C.; Miguel Pruneda, J.; Hayashi, N.; Watanabe, T.; Kitada, A.; Tsujimoto, Y.; Kageyama, H.; Yoshimura, K.; Takano, M.; Nishi, M.; Ohoyama, K.; Mizumaki, M.; Kawamura, N.; Iniguez, J.; Canadell, E. *J. Am. Chem. Soc.* **2009**, *131*, 221−229.

(8) Yajima, T.; Kitada, A.; Kobayashi, Y.; Sakaguchi, T.; Bouilly, G.; Kasahara, S.; Terashima, T.; Takano, M.; Kageyama, H. *J. Am. Chem. Soc.* **2012**, *134*, 8782−8785.

(9) Huan, G.; Greenblatt, M.; Croft, M. *Eur. J. Solid State Inorg. Chem.* **1989**, *26*, 193−220.

(10) Oledzka, M.; Lee, J.-G.; Ramanujachary, K.; Greenblatt, M. *J. Solid State Chem.* **1996**, *127*, 151−160.

(11) Oledzka, M.; Ramanujachary, K.; Greenblatt, M. *Mater. Res. Bull.* **1998**, *33*, 855−866.

(12) Borg, C. K. H.; Zhou, X.; Eckberg, C.; Campbell, D. J.; Saha, S. R.; Paglione, J.; Rodriguez, E. E. *Phys. Rev. B: Condens. Matter Mater. Phys.* **2016**, *93*, 094522.

(13) Zhou, X.; Borg, C. K. H.; Lynn, J. W.; Saha, S. R.; Paglione, J.; Rodriguez, E. E. *J. Mater. Chem. C* **2016**, *4*, 3934−3941.

(14) Zhou, X.; Eckberg, C.; Wilfong, B.; Liou, S.-C.; Vivanco, H. K.; Paglione, J.; Rodriguez, E. *arXiv preprint* **2016**, arXiv:1611.02383.

(15) Vivanco, H. K.; Rodriguez, E. E. *J. Solid State Chem.* **2016**, *242*, 3−21.

(16) Burrard-Lucas, M.; Free, D. G.; Sedlmaier, S. J.; Wright, J. D.; Cassidy, S. J.; Hara, Y.; Corkett, A. J.; Lancaster, T.; Baker, P. J.; Blundell, S. J.; Clarke, S. J. *Nat. Mater.* **2013**, *12*, 15−19.

(17) Hatakeda, T.; Noji, T.; Kawamata, T.; Kato, M.; Koike, Y. *J. Phys. Soc. Jpn.* **2013**, *82*, 123705.

(18) Lu, X. F.; Wang, N. Z.; Zhang, G. H.; Luo, X. G.; Ma, Z. M.; Lei, B.; Huang, F. Q.; Chen, X. H. *Phys. Rev. B: Condens. Matter Mater. Phys.* **2014**, *89*, 020507.

(19) Sun, H.; et al. *Inorg. Chem.* **2015**, *54*, 1958−1964.

(20) Kovnir, K.; Garlea, V. O.; Thompson, C. M.; Zhou, H.; Reiff, W. M.; Ozarowski, A.; Shatruk, M. *Inorg. Chem.* **2011**, *50*, 10274−10283.

(21) Kovnir, K.; Reiff, W. M.; Menushenkov, A. P.; Yaroslavtsev, A. A.; Chernikov, R. V.; Shatruk, M. *Chem. Mater.* **2011**, *23*, 3021−3024.

(22) Thompson, C. M.; Kovnir, K.; Garlea, V. O.; Choi, E. S.; Zhou, H. D.; Shatruk, M. *J. Mater. Chem. C* **2014**, *2*, 7561−7569.

(23) Menushenkov, A. P.; Yaroslavtsev, A. A.; Geondzhian, A. Y.; Chernikov, R. V.; Zubavichus, Y. V.; Tan, X.; Shatruk, M. *J. Supercond. Novel Magn.* **2015**, *28*, 995−997.

(24) Tan, X.; Fabbris, G.; Haskel, D.; Yaroslavtsev, A. A.; Cao, H.; Thompson, C. M.; Kovnir, K.; Menushenkov, A. P.; Chernikov, R. V.; Garlea, V. O.; Shatruk, M. *J. Am. Chem. Soc.* **2016**, *138*, 2724−2731.

(25) Hoffmann, R.; Zheng, C. *J. Phys. Chem.* **1985**, *89*, 4175−4181.

(26) Hoffmann, R. *Angew. Chem., Int. Ed. Engl.* **1987**, *26*, 846−878.

(27) Cheary, R. W.; Coelho, A. *J. Appl. Crystallogr.* **1992**, *25*, 109−121.

DOI: 10.1021/jacs.6b10229
J. Am. Chem. Soc. 2016, 138, 16432−16442

(28) Hohenberg, P.; Kohn, W. *Phys. Rev.* **1964**, *136*, B864−B871.
(29) Kohn, W.; Sham, L. J. *Phys. Rev.* **1965**, *137*, A1697−A1705.
(30) Kresse, G. Ph.D. thesis, Technische Universiät Wien, 1993.
(31) Kresse, G.; Hafner, J. *Phys. Rev. B: Condens. Matter Mater. Phys.* **1993**, *47*, 558−561.
(32) Kresse, G.; Furthmüller, J. *Comput. Mater. Sci.* **1996**, *6*, 15−50.
(33) Kresse, G.; Furthmüller, J. *Phys. Rev. B: Condens. Matter Mater. Phys.* **1996**, *54*, 11169−11186.
(34) Blöchl, P. E. *Phys. Rev. B: Condens. Matter Mater. Phys.* **1994**, *50*, 17953−17979.
(35) Perdew, J. P.; Burke, K.; Ernzerhof, M. *Phys. Rev. Lett.* **1996**, *77*, 3865−3868.
(36) Monkhorst, H. J.; Pack, J. D. *Phys. Rev. B* **1976**, *13*, 5188−5192.
(37) Dronskowski, R.; Bloechl, P. E. *J. Phys. Chem.* **1993**, *97*, 8617−8624.
(38) Deringer, V. L.; Tchougréeff, A. L.; Dronskowski, R. *J. Phys. Chem. A* **2011**, *115*, 5461−5466.
(39) Maintz, S.; Deringer, V. L.; Tchougréeff, A. L.; Dronskowski, R. *J. Comput. Chem.* **2013**, *34*, 2557−2567.
(40) Maintz, S.; Deringer, V. L.; Tchougréeff, A. L.; Dronskowski, R. *J. Comput. Chem.* **2016**, *37*, 1030−1035.
(41) Komarek, K. L.; Wessely, K. *Monatsh. Chem.* **1972**, *103*, 896−906.
(42) Bøhm, F.; Grøvold, F.; Haraldsen, H.; Pyrdz, H. *Acta Chem. Scand.* **1955**, *9*, 1510.
(43) Yang, J.; Chen, B.; Wang, H.; Mao, Q.; Imai, M.; Yoshimura, K.; Fang, M. *Phys. Rev. B: Condens. Matter Mater. Phys.* **2013**, *88*, 064406.
(44) Jeitschko, W.; Meisen, U.; Möller, M. H.; Reehuis, M. Z. *Z. Anorg. Allg. Chem.* **1985**, *527*, 73−84.
(45) Kaul, S. N. *J. Phys.: Condens. Matter* **1999**, *11*, 7597.
(46) Motohashi, T.; Ono, T.; Sugimoto, Y.; Masubuchi, Y.; Kikkawa, S.; Kanno, R.; Karppinen, M.; Yamauchi, H. *Phys. Rev. B: Condens. Matter Mater. Phys.* **2009**, *80*, 165114.
(47) Moriya, T. *J. Magn. Magn. Mater.* **1979**, *14*, 1−46.
(48) Ueda, K.; Moriya, T. *J. Phys. Soc. Jpn.* **1975**, *39*, 605−615.
(49) Neilson, J. R.; McQueen, T. M. *J. Am. Chem. Soc.* **2012**, *134*, 7750−7757.
(50) Greenfield, J. T.; Kamali, S.; Lee, K.; Kovnir, K. *Chem. Mater.* **2015**, *27*, 588−596.
(51) Gamble, F. R.; DiSalvo, F. J.; Klemm, R. A.; Geballe, T. H. *Science* **1970**, *168*, 568−570.
(52) Gamble, F. R.; Osiecki, J. H.; Cais, M.; Pisharody, R.; DiSalvo, F. J.; Geballe, T. H. *Science* **1971**, *174*, 493−497.
(53) Sedlmaier, S. J.; Cassidy, S. J.; Morris, R. G.; Drakopoulos, M.; Reinhard, C.; Moorhouse, S. J.; O'Hare, D.; Manuel, P.; Khalyavin, D.; Clarke, S. J. *J. Am. Chem. Soc.* **2014**, *136*, 630−633.
(54) Ying, T.; Chen, X.; Wang, G.; Jin, S.; Zhou, T.; Lai, X.; Zhang, H.; Wang, W. *Sci. Rep.* **2012**, *2*, 426.
(55) Jin, S.; Wu, X.; Huang, Q.; Wu, H.; Ying, T.; Fan, X.; Sun, R.; Zhao, L.; Chen, X. *arXiv preprint* **2016**, arXiv:1607.01103.
(56) Stoner, E. C. *Proc. R. Soc. London, Ser. A* **1938**, *165*, 372−414.
(57) Ding, Y.; Wang, Y.; Ni, J. *Solid State Commun.* **2009**, *149*, 505−509.
(58) Liu, D.; et al. *Nat. Commun.* **2012**, *3*, 931.
(59) Ge, J.-F.; Liu, Z.-L.; Liu, C.; Gao, C.-L.; Qian, D.; Xue, Q.-K.; Liu, Y.; Jia, J.-F. *Nat. Mater.* **2015**, *14*, 285−289.
(60) Certain commercial equipment, instruments, or materials are identified in this document. Such identification does not imply recommendation or endorsement by the National Institute of Standards and Technology nor does it imply that the products identified are necessarily the best available for the purpose.

DOI: 10.1021/jacs.6b10229
J. Am. Chem. Soc. 2016, 138, 16432−16442